

The nonlinear initiation of side-branching by activator-inhibitor (Turing) morphogenesis

Arik Yochelis^{1,2}

¹Department of Solar Energy and Environmental Physics,
Blaustein Institutes for Desert Research (BIDR), Ben-Gurion University of the Negev,
Sede Boqer Campus, Midreshet Ben-Gurion 8499000, Israel

²Department of Physics, Ben-Gurion University of the Negev, Be'er Sheva 8410501, Israel

An understanding of the underlying mechanism of side-branching is paramount to control and/or potentially form mammalian organs, such as lungs, kidneys, and glands. Motivated by an activator-inhibitor approach that is believed to dominate the initiation of side-branching, I show that the mechanism stems from the nonlinear (subcritical) Turing bifurcation to periodic and spatially localized solutions that are essential for excitation at the differentiation-front propagation. The results demonstrate a distinct robust mechanism of side-branching through numerical analysis of model equations that have been employed to study branching in the lungs.

Several essential epithelial-based organs in mammals, such as the lungs, kidneys, pancreas, and mammary glands, self-organize in tree-like branched architectures, a form that assists in exploiting a large active surface area while preserving a small volume [1–14]. While the mechanism of side-branching remains obscured due to multiscale processes that range from molecular to tissue levels [15], recent experimental studies indicate that biochemical signaling at the mesoscale is the dominant feature in the initiation of branches [3, 9, 14, 16–21], i.e., roughly speaking the interactions between proteins, ligands and receptors, e.g., similar signaling paths (albeit with distinct subsets) were drawn for ingrowths of the lung, salivary gland and kidney [11]. Specifically, this work is motivated by suppression of side-branches in the lungs upon addition of matrix GLA protein (MGP), which is the inhibitor of the bone morphogenetic protein (BMP) activator [3], as shown in the reused Fig. 1.

Biochemical circuits often point towards Turing's morphogenesis mechanism [22] as a plausible activator-inhibitor (AI) modeling framework also for the branching mechanism, ranging from mammalian organs to plant roots [3, 14, 23–25]. However, although numerical simulations show a similarity to empirically observed branched dichotomy [5, 13, 26–32], the explicit mechanism remains hindered, especially for side-branching nucleation [15]. The main barrier is the linearity of Turing's mechanism that is valid for infinitesimal perturbations and short time scales, whereas peaks and fronts are beyond these limits [33].

In this Letter, I use an activator-inhibitor model that has been employed in the context of lungs development [3], to reveal the side-branching nucleation mechanism. I show that spatially localized peaks that arise in a subcritical Turing bifurcation are those that initiate side-branching upon differentiation-front propagation. Due to the relatively cumbersome form of the model equations, the study mostly involves bifurcation analysis via the numerical path continuation method in one-

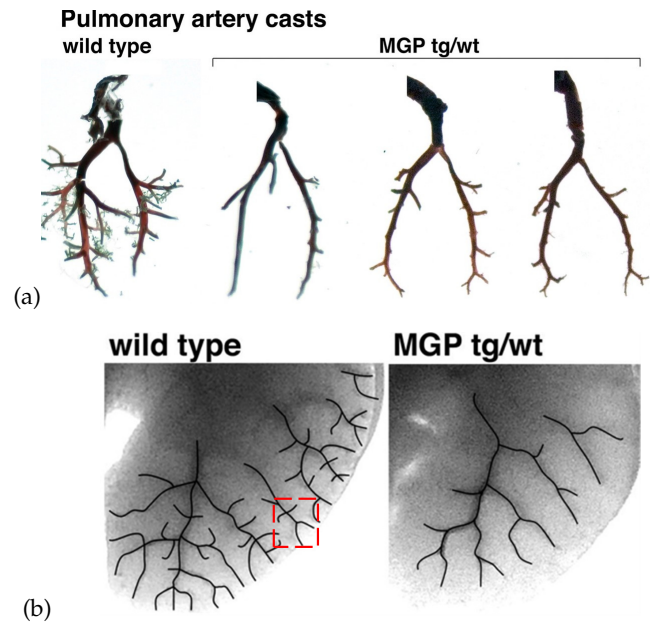


FIG. 1. (a) Lung morphology casts and (b) pulmonary vascular pattern from wild type littermates and MGP transgenic mice. The dashed-line rectangle in (b) demonstrates side-branching (dark lines), where segments evolve perpendicular to the main branch in contrast to splitting that follows a Y-shape dichotomy. This research was originally published in the *Journal of Biological Chemistry* [3] the American Society for Biochemistry and Molecular Biology.

space dimensions (1D) and validations by direct numerical simulations (DNS) in 1D and 2D. In the end, I discuss possible implications that could shed new light on other biochemical feedbacks, where side-branching is needed (e.g., mammalian organs and plant roots) or inhibit them when it is known to be notorious (e.g., metastasis).

I start the study with AI model equations that have been proposed by Meinhardt in 1976 [34] as a branching framework and later on employed in the context of

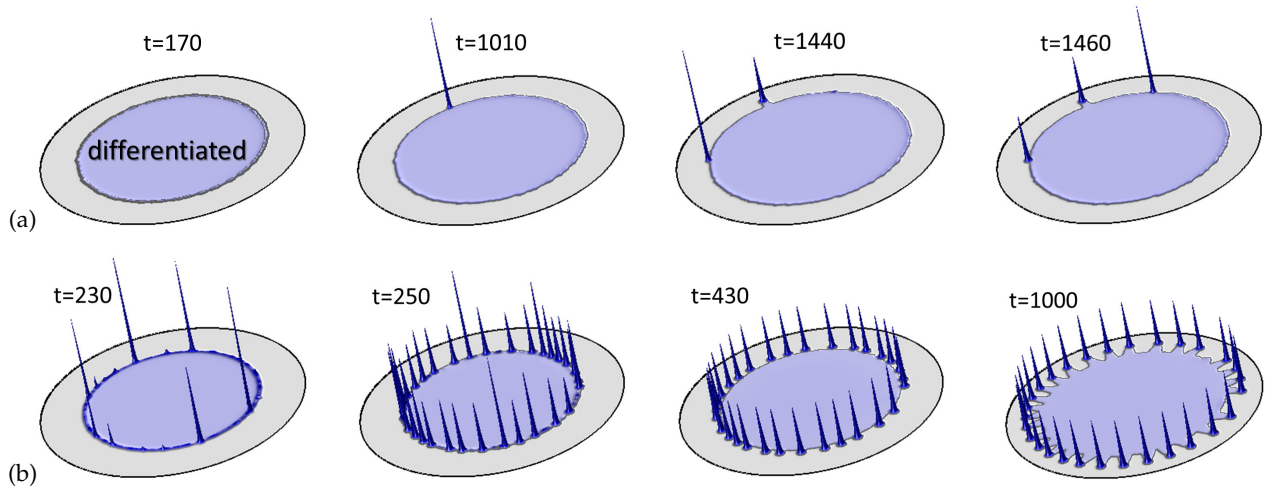


FIG. 2. Snapshots of DNS of (1) showing the activator field, A , computed on a circular domain of diameter 30 and Neumann boundary conditions, where the initial condition is a circular domain with a diameter of about 20; dark color indicates higher values of A and differentiated Y . Parameters: (a) $\rho_H = 3.0 \cdot 10^{-5}$ and (b) $\rho_H = 2.5 \cdot 10^{-5}$.

pulmonary vascular and lung development [3]

$$\begin{aligned} \frac{\partial A}{\partial t} &= F_A(A, H, S, Y) + D_A \nabla^2 A, \\ \frac{\partial H}{\partial t} &= F_H(A, H, S, Y) + D_H \nabla^2 H, \\ \frac{\partial S}{\partial t} &= F_S(S, Y) + D_S \nabla^2 S, \quad \frac{\partial Y}{\partial t} = F_Y(A, Y), \end{aligned} \quad (1)$$

where $F_A = cSA^2/H - \mu A + \rho_A Y$, $F_H = cSA^2 - \nu H + \rho_H Y$, $F_S = c_0 - \gamma S - \varepsilon Y S$, $F_Y = dA - eY + Y^2/(1 + fY^2)$. In (1) A , H , and S are diffusible concentrations of activator (BMP), inhibitor (MGP), and substrate, respectively, while the Y represents an irreversible marker for cell differentiation that is generated solely by the activator. For a detailed description of the biochemical signaling the reader is referred to [3]. Following the experimental results [3], I also use the inhibitor secreted by cells, ρ_H , as a control parameter while keeping all other parameters fixed: $c = 0.002$, $\mu = 0.16$, $\rho_A = 0.005$, $\nu = 0.04$, $c_0 = 0.02$, $\gamma = 0.02$, $\varepsilon = 0.1$, $d = 0.008$, $e = 0.1$, $f = 10$, $D_A = 0.001$, $D_H = 0.02$, $D_S = 0.01$. I note that no fluctuations in parameter values are employed and at the end I explain their need in [3, 29, 34].

Previous studies of Eqs. 1 have explored numerically the phenomenology of branching in 2D and 3D [28, 31, 32] and in some cases linear analysis was also incorporated to gain insights [29, 30]. The most prominent feature of these works is propagation of new branches which are characterized by a peak shape activator concentration at the front of the differentiated marker (i.e., outside the Turing unstable region). The spatially localized concentrations have been identified as propagating peaks. However, it should be emphasized that unlike typical propagating solitary waves (e.g., excitable pulses) that biasymptote in space to the same rest state,

localized solutions of (1) are in fact fronts with an overshoot structure, bearing a similarity to actin polymerization that manifests the dynamics of circular dorsal ruffles [35]. Next, I show that in addition to these fronts (with an overshoot form), these are the 1D coexisting stationary periodic and localized solutions on top of the uniform activator that trigger the 2D side-branching.

To demonstrate the nucleation phenomenology, I initialize DNS with a front-like solution for two values of ρ_H , as shown in Fig. 2. (To eliminate the effects of boundary conditions, the phenomenon is demonstrated on circular domains.) For the high value of ρ_H there are a few nucleations of peaks that appear without a specific length scale, after a relatively long period of time, as shown in Fig. 2(a). At the nucleation, the peak amplitudes are the largest and then they saturate through the side-branch propagation, e.g., times $t = 1440$ and $t = 1460$. As ρ_H is decreased, the nucleation starts at a much earlier time ($t = 230$) and the forming peaks become separated in specific spatial scale along the circumference, see $t = 250$ in Fig 2(b). After the initial nucleation no additional nucleations occur and the side-branches form a ‘‘corona-type’’ shape during their propagation, see $t = 1000$. The former case implies, in general, absence of side-branching the latter case supports side-branching, consistently with [3] (although here no fluctuations in c_0 were used). Thus, to reveal the origin behind this nucleation mechanism and relating it to side branching, a nonlinear analysis is performed in what follows.

I start the analysis by solving (1) for uniform solutions. In addition to the ‘trivial’ stable solution $(A, H, S, Y) = (0, 0, c_0/\gamma, 0)$ there are additional regions in which further three or five nontrivial solutions coexist of which only one is stable (marked by the solid line

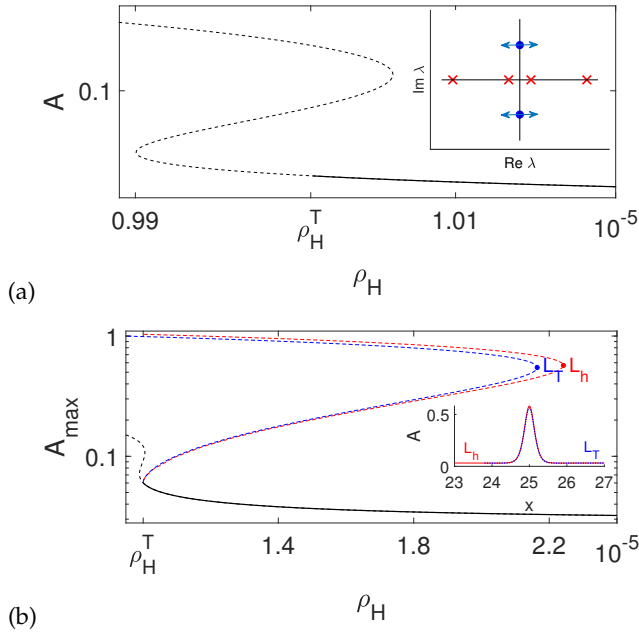


FIG. 3. (a) Bifurcation diagram showing the activator values, A , and the Turing instability onset, $\rho_H^T \simeq 1.01 \cdot 10^{-5}$, where the inset depicts the configuration of the spatial eigenvalues (λ) at the onset according to (2) about the uniform solution. Solid/dashed lines mark stable/unstable solutions. (b) Bifurcation diagram for nonuniform periodic ($L_T \simeq 2.89$) and localized ($L_h = 50$) solutions that bifurcate from the Turing onset, $\rho_H = \rho_H^T$, computed via path continuation [36] of (2); a logarithmic scale is used for A_{\max} . The inset shows the respective profiles at saddle-nodes that are marked by ‘•’.

in Fig. 3(a), while other solutions are not shown). The region of interest is thus related to loss of stability of the nontrivial solution. Next, I turn to the emergence of spatially nonuniform solutions from the nontrivial uniform solution by identifying, via standard linear analysis to periodic infinitesimal perturbations [37], the Turing (finite wavenumber) instability onset $\rho_H = \rho_H^T$, see Fig. 3(a). To obtain the nonuniform solutions of (1) and their organization, I exploit the spatial dynamics method, i.e., I seek steady-state solutions by removing the time derivatives and rewrite (1) as first-order differential equations in space and add a weak diffusion for the Y field ($D_Y = 10^{-7} \ll D_A$) for numerical regularity:

$$\begin{aligned} A_x &= -a, & a_x &= F_A(A, H, S, Y)/D_A, \\ H_x &= -h, & h_x &= F_H(A, H, S, Y)/D_H, \\ S_x &= -s, & s_x &= F_S(S, Y)/D_S, \\ Y_x &= -y, & y_x &= F_Y(A, Y)/D_Y. \end{aligned} \quad (2)$$

Although stability of the steady-state solutions is of a lesser importance here, it is complemented by standard eigenvalue computations using (1).

Using (2), I numerically obtain (using path-continuation package AUTO [36]) the primary branch

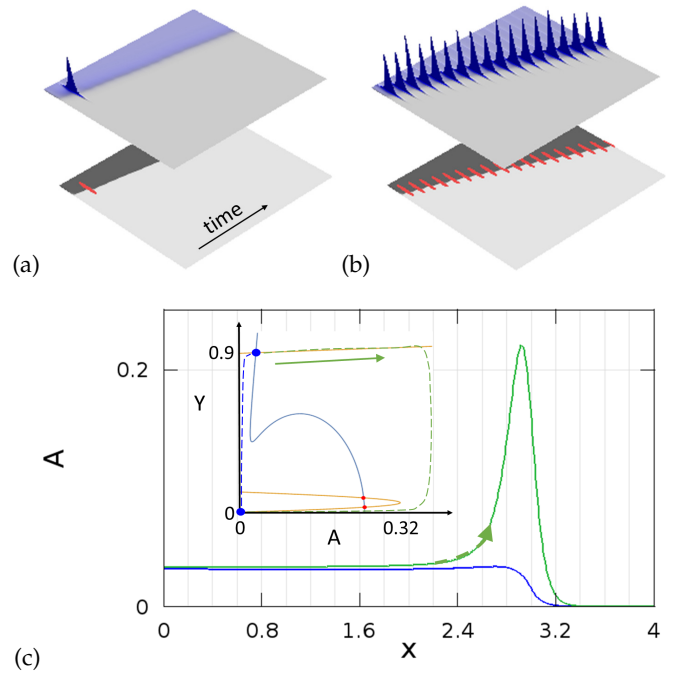


FIG. 4. Space-time DNS of (1) showing both the activator A (top) and cell differentiation Y (bottom) fields for: (a) $\rho_H = 3.0 \cdot 10^{-5}$ and (b) $\rho_H = 2.0 \cdot 10^{-5}$, where non-uniform solutions coexist. DNS was performed on a spatial domain $x \in [0, 5]$ and times $t \in [0, 3000]$; dark color indicates higher values of both fields and the (red) dashes at the bottom mark the relative locations of the activator peaks. Boundary conditions are Neumann and the initial condition is a front at $x = 0.5$. (c) Two front profiles are taken from Fig. 4(b), showing a solution before peak formation (dark/blue line, time 2910) and at the beginning of peak formation (light/green line, time 2996). The inset shows the nullclines of (1) in the $A - Y$ plane, the unstable fixed points (light/red ‘•’), stable fixed points (dark/blue ‘•’), and the heuristic trajectory of fronts (dashed lines), where the left trajectory corresponds to bottom profile; the arrow indicates the direction of the peak as also indicated in the main figure by the dashed arrow at the top profile.

of bifurcating Turing solutions, i.e., solutions with periodicity $L_T = 2\pi/k_T \simeq 2.89$, where k_T is the critical wavenumber at the onset $\rho_H = \rho_H^T$. The periodic solutions, L_T , bifurcate subcritically, that is, towards the stable direction of the uniform state (see Fig. 3(b)), and are unstable (marked by the dark dashed line). Typically, periodic solutions of Turing type are accompanied by spatially localized solutions (homoclinic connections in space) that organize in a “snakes and ladders” structure [38]. By performing continuation on large domains, $L_h \gg L_T$, I indeed find periodic solutions (light line) but these are only single-peak states and do not form a typical homoclinic snaking structure. Homoclinic snaking phenomena [39] (including AI media [40, 41]) stems from the Hamiltonian-Hopf bifurcation in space, where the configuration of the spatial eigenvalues corresponds to a double multiplicity at the imaginary

axis, cf. [42, 43]. For system (2), linearization about the stable uniform state, leads to eight spatial eigenvalues (λ) of which four indeed show double multiplicity at the imaginary axis (marked by ‘•’) while the other four are real (marked by ‘×’), as shown in the inset of Fig. 3(a). The arrows indicate the direction of the splitting of the imaginary eigenvalues (marked by ‘•’) for $\rho_H > \rho_H^T$ while for $\rho_H < \rho_H^T$ the splitting occurs on the imaginary axis. I note that in this region there are additional coexisting solutions and additional details but the interest here is solely in the side-branching mechanism so that a more complete analysis will be conducted elsewhere, through analysis about Hamiltonian–Hopf and Belyakov–Devaney bifurcations [44]. The saddle-node (SN) of localized solutions (labeled as L_h) extends beyond the existence region of periodic Turing states (L_T), i.e., for larger values of ρ_H . The inset in Fig. 3(b) shows that the periodic and the localized solutions have the same form, although $L_T \ll L_h$, as demonstrated via the profiles at both SN. Notably, other periodic solutions also coexist in this range, up to the SN of L_h .

The existence of spatially periodic and localized solutions in 1D is related to the nucleation phenomenology in 2D that were demonstrated in Fig. 2. To show this connection, I first demonstrate how a 1D front propagation looks like, see Fig. 4. For a high value of ρ_H that is outside the coexistence region of localized solutions, DNS show that a single peak forms at early times and then propagation of a front is without an overshoot (Fig. 4(a)). For ρ_H values that are within the subcritical Turing regime (Fig. 4(b)), front propagation involves localized oscillations at the front line. These are manifestations of the AI kinetics and can be deduced using the nullclines, i.e., in the (A, Y) plane with invariant manifolds $F_A = F_H = 0$. In Fig. 4(c), I plot two front profiles, one before peak formation (bottom line) and the other through the peak formation (top line) while in the inset plotting the nullclines (solid lines) along with heuristic trajectories (dashed lines) of the spatial solution in the (A, Y) plane. Front propagation increases locally A due to jump in Y , therefore, if ρ_H is in the subcritical Turing region, the trajectory goes above the top nullcline (as indicated in the inset by the arrow) along the manifold of the spatially localized solution. Since, the peak height is about $A_{\max} \simeq 0.5$ (see inset in Fig. 3(b)), the trajectory makes a large excursion (the overshoot) before connecting to the trivial state at $(A, Y)=(0,0)$. In the absence of such peaks, the perturbation falls on the left trajectory and connects to the trivial state and thus, has the profile does not show any overshoot. The peak is unstable at the front line and its decay is associated with fast inhibition transport for which the large excursion decreases along the top nullcline (in a reversed direction) to restore a front solution without an overshoot. The latter behavior different from a with two-variable AI system [45]. Note that the first nucleations in 1D

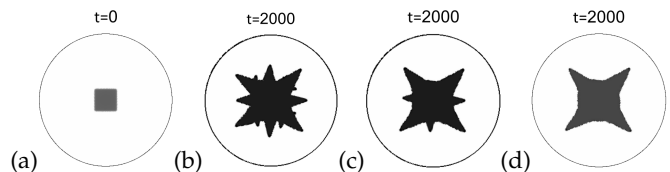


FIG. 5. Snapshots of DNS of (1) showing the cell differentiation field, Y , computed on a circular domain (as in Fig. 2) with Neumann boundary conditions, where the initial condition depicted in (a); dark color indicates higher values of Y . Parameters: (b) $\rho_H = 2.0 \cdot 10^{-5}$, (c) $\rho_H = 2.5 \cdot 10^{-5}$, (d) $\rho_H = 3.0 \cdot 10^{-5}$.

occur at about the same time as for the 2D case, about $t = 200$ (see Fig. 2(b)). The periodicity of the coexisting 1D solutions is also manifested in the length scale of the peaks at the circumference (see Fig. 2(b)) while outside the subcritical regime nucleation may still occur but it would be through singular events as in Fig. 2(a)).

Finally, I turn to validation via 2D DNS at the $\rho_H > \rho_H^T$ regime. To generalize the impact of front solutions, I initialize the DNS with a relatively small square seed, as shown in Fig. 5(a). Specifically, this initial condition has well defined high curvature regions that force the branching initiations. While the existence regions in 2D need not coincide with the 1D [46, 47], the qualitative behavior still persists. In Figs. 5(b-d), I show that near the Turing onset, the development of side-branches emerges spontaneously (see (b,c)), where the time to side-branch initiation increases with distance from the Turing’s onset. Outside the subcritical Turing regime the side-branches are inhibited, as shown in Fig. 3(d).

To conclude, using the numerical bifurcation analysis of activator–inhibitor system in 1D, I showed that the nucleation mechanism of side-branches is related to the interplay between a front propagation and a nonlinear (Turing) instability to nonuniform solutions (spatially periodic or localized), where periodic solutions indicate the spatial length scale at which side-branches appear. Outside the coexistence region of nonuniform solutions, where the inhibition (in (1) by cell differentiation) is large enough, side-branching is suppressed. While focusing here on a relatively narrow parameter region, the obtained results reflect on theoretical implications that are known to exist in other parameter choices. For example, the subcritical nature of the Turing instability explains the need for parameter fluctuations that were obtained in previous DNS of (1) [34], i.e., fluctuations of c_0 lead to large perturbations about the trivial state that in turn produce side branching and form patterns as in Fig. 1(b) [3, 29]. Moreover, the results open intriguing questions about the homoclinic snaking phenomenon that exhibits both complex and real spatial eigenvalues, yet, these are beyond the scope of this paper and will be discussed elsewhere.

While control over the side-branching mechanism is essential to the development of organs [15], suppression of side-branching however, can provide insights into pathologies related to cancer, such as the relevance of epithelial/mesenchymal phenotypes transition to metastasis [48–51]. More broadly, it can be speculated that the activator–inhibitor insights can be incorporated into the formation of plant roots [52, 53], formation of somites [54] and into inhibition of spike peplomers in coronaviruses (e.g., COVID-19) [55] or budding morphogenesis in influenza [56].

I am grateful to Prof. Ehud Meron (BGU) for his insightful comments on the manuscript and to Prof. Edgar Knobloch (UC Berkeley) for helpful discussions on homoclinic snaking.

-
- [1] J. Caduff, L. Fischer, and P. H. Burri, *The Anatomical Record* **216**, 154 (1986).
- [2] M. Roth-Kleiner, T. M. Berger, M. R. Tarek, P. H. Burri, and J. C. Schittny, *Developmental dynamics: an official publication of the American Association of Anatomists* **233**, 1261 (2005).
- [3] Y. Yao, S. Nowak, A. Yochelis, A. Garfinkel, and K. I. Boström, *Journal of Biological Chemistry* **282**, 30131 (2007).
- [4] D. Warburton, *Nature* **453**, 733 (2008).
- [5] R. J. Metzger, O. D. Klein, G. R. Martin, and M. A. Krasnow, *Nature* **453**, 745 (2008).
- [6] P. Lu and Z. Werb, *Science* **322**, 1506 (2008).
- [7] M. Affolter, R. Zeller, and E. Caussinus, *Nature Reviews Molecular Cell Biology* **10**, 831 (2009).
- [8] F. Costantini and R. Kopan, *Developmental Cell* **18**, 698 (2010).
- [9] Y. Yao, M. Jumabay, A. Wang, and K. I. Boström, *The Journal of Clinical Investigation* **121**, 2993 (2011).
- [10] M. H. Little and A. P. McMahon, *Cold Spring Harbor Perspectives in Biology* **4**, a008300 (2012).
- [11] D. Iber and D. Menshykau, *Open Biology* **3**, 130088 (2013).
- [12] J. Davies, in *Principles of Developmental Genetics* (Elsevier, 2015) pp. 255–264.
- [13] E. Hannezo, C. L. Scheele, M. Moad, N. Drogo, R. Heer, R. V. Sampogna, J. Van Rheenen, and B. D. Simons, *Cell* **171**, 242 (2017).
- [14] D. Menshykau, O. Michos, C. Lang, L. Conrad, A. P. McMahon, and D. Iber, *Nature Communications* **10**, 1 (2019).
- [15] E. Hannezo and B. D. Simons, *Current Opinion in Cell Biology* **60**, 99 (2019).
- [16] K. Sainio, P. Suvanto, J. Davies, J. Wartiovaara, K. Wartiovaara, M. Saarna, U. Arumae, X. Meng, M. Lindahl, V. Pachnis, *et al.*, *Development* **124**, 4077 (1997).
- [17] M.-J. Tang, D. Worley, M. Sanicola, and G. R. Dressler, *The Journal of Cell Biology* **142**, 1337 (1998).
- [18] D. Lebeche, S. Malpel, and W. V. Cardoso, *Mechanisms of Development* **86**, 125 (1999).
- [19] M.-J. Tang, Y. Cai, S.-J. Tsai, Y.-K. Wang, and G. R. Dressler, *Developmental Biology* **243**, 128 (2002).
- [20] K. A. Gilbert and S. R. Rannels, *American Journal of Physiology-Lung Cellular and Molecular Physiology* **286**, L1179 (2004).
- [21] M. Hagiwara, F. Peng, and C.-M. Ho, *Scientific Reports* **5**, 8054 (2015).
- [22] J. H. Dawes, *Historia Mathematica* **43**, 49 (2016).
- [23] A. Jilkine, A. F. Marée, and L. Edelstein-Keshet, *Bulletin of Mathematical Biology* **69**, 1943 (2007).
- [24] R. J. Payne and C. S. Grierson, *PLoS One* **4** (2009).
- [25] P. Krupinski, B. Bozorg, A. Larsson, S. Pietra, M. Grebe, and H. Jönsson, *Frontiers in Plant Science* **7**, 1560 (2016).
- [26] D. Menshykau, C. Kraemer, and D. Iber, *PLoS Computational Biology* **8** (2012).
- [27] G. Cellière, D. Menshykau, and D. Iber, *Biology Open* **1**, 775 (2012).
- [28] Y. Guo, T.-H. Chen, X. Zeng, D. Warburton, K. I. Boström, C.-M. Ho, X. Zhao, and A. Garfinkel, *The Journal of Physiology* **592**, 313 (2014).
- [29] Y. Guo, M. Sun, A. Garfinkel, and X. Zhao, *PloS One* **9** (2014).
- [30] H. Xu, M. Sun, and X. Zhao, *PloS One* **12** (2017).
- [31] G. Shan, H. Chuan-shan, S. Ming-zhu, and Z. Xin, *Journal of Theoretical Biology* **455**, 293 (2018).
- [32] X. Zhu and H. Yang, *Micromachines* **9**, 109 (2018).
- [33] A. Doelman, *Complexity Science*, 129 (2019).
- [34] H. Meinhardt, *Differentiation* **6**, 117 (1976).
- [35] E. Bernitt, H.-G. Döbereiner, N. S. Gov, and A. Yochelis, *Nature Communications* **8**, 15863 (2017).
- [36] E. J. Doedel *et al.*, “Auto07p: Continuation and bifurcation software for ordinary differential equations,” (2012).
- [37] M. Cross and P. Hohenberg, *Reviews of Modern Physics* **65**, 851 (1993).
- [38] J. Burke and E. Knobloch, *Physics Letters A* **360**, 681 (2007).
- [39] D. Avitabile, D. J. Lloyd, J. Burke, E. Knobloch, and B. Sandstede, *SIAM Journal on Applied Dynamical Systems* **9**, 704 (2010).
- [40] A. Yochelis, Y. Tintut, L. Demer, and A. Garfinkel, *New Journal of Physics* **10**, 055002 (2008).
- [41] V. Breña-Medina and A. Champneys, *Physical Review E* **90**, 032923 (2014).
- [42] A. R. Champneys, *Physica D* **112**, 158 (1998).
- [43] E. Knobloch, *Annu. Rev. Condens. Matter Phys.* **6**, 325 (2015).
- [44] P. Parra-Rivas, D. Gomila, L. Gelens, and E. Knobloch, *Physical Review E* **97**, 042204 (2018).
- [45] A. Yochelis and A. Garfinkel, *Physical Review E* **77**, 035204 (2008).
- [46] D. J. Lloyd, B. Sandstede, D. Avitabile, and A. R. Champneys, *SIAM Journal on Applied Dynamical Systems* **7**, 1049 (2008).
- [47] N. Gavish, I. Versano, and A. Yochelis, *SIAM Journal on Applied Dynamical Systems* **16**, 1946 (2017).
- [48] M.-Y. Lee and M.-R. Shen, *American Journal of Translational Research* **4**, 1 (2012).
- [49] M. K. Jolly, M. Boareto, B. Huang, D. Jia, M. Lu, E. Ben-Jacob, J. N. Onuchic, and H. Levine, *Frontiers in Oncology* **5**, 155 (2015).
- [50] M. Garg, *Expert Reviews in Molecular Medicine* **19** (2017).
- [51] T.-T. Liao and M.-H. Yang, *Cells* **9**, 623 (2020).
- [52] V. Breña-Medina, A. R. Champneys, C. Grierson, and M. J. Ward, *SIAM Journal on Applied Dynamical Systems* **13**, 210 (2014).
- [53] D. Draelants, D. Avitabile, and W. Vanroose, *Journal of*

- The Royal Society Interface **12**, 20141407 (2015).
- [54] R. E. Baker, S. Schnell, and P. K. Maini, *Current Topics in Developmental Biology* **81**, 183 (2008).
- [55] T. C. Hobman, *Trends in Microbiology* **1**, 124 (1993).
- [56] D. P. Nayak, R. A. Balogun, H. Yamada, Z. H. Zhou, and S. Barman, *Virus Research* **143**, 147 (2009).